

# Ten-Ampere-Level, Applied-Field-Dominant Operation in Magnetoplasmadynamic Thrusters

Daisuke Ichihara,\* Tomoki Uno,† Hisashi Kataoka,‡ Jaehun Jeong,† Akira Iwakawa,‡ and Akihiro Sasoh§

Nagoya University, Nagoya 464-8603, Japan

DOI: 10.2514/1.B36179

In this paper, applied-field magnetoplasmadynamic thrusters were operated with a discharge current lower than 20 A and an argon propellant flow rate under 4.0 mg/s by using a thermionic electron emission-type hollow cathode. Both axisymmetric and rectangular channel configurations were examined. The characteristic value of the ratio of the applied-field electromagnetic thrust to the self-field electromagnetic thrust, which was a maximum of approximately 50 in previous research, increased to more than 800 in this study, whereas the specific power was in approximately the same range as in previous studies. The trends of thrust and discharge voltage were explained by referring to the “swirl acceleration” model. Such operation could be useful for near-future high-power electric propulsion applications.

## Nomenclature

$a_0$	= ion acoustic speed, m/s
$\mathbf{B}$	= magnetic field vector, T
$B$	= magnetic field strength, T
$c$	= coefficient
$\mathbf{E}$	= electric field vector, V/m
$F$	= thrust, N
$F_A$	= representative value of applied-field thrust, N
$F_{\text{EXP}}$	= experimentally measured thrust, N
$F_S$	= representative value of self-field thrust, N
$F_{\text{RR}}$	= thrust by rigid rotator model, N
$F_{\text{tare}}$	= tare force, N
$F_{\text{TKV}}$	= thrust by Tikhonov’s model, N
$g$	= gravitational acceleration, m/s <sup>2</sup>
$H$	= interelectrode distance in type B thrusters, m
$I_{\text{sp}}$	= specific impulse, s
$\mathbf{j}$	= discharge current density, A/m <sup>2</sup>
$J_d$	= discharge current, A
$J_k$	= keeper current, A
$k$	= Boltzmann constant, m <sup>2</sup> · kg/s <sup>2</sup> · K
$M_i$	= ion mass, kg
$\dot{m}$	= total propellant mass flow rate, kg/s
$\dot{m}_1$	= propellant mass flow rate through hollow cathode, kg/s
$\dot{m}_2$	= propellant mass flow rate outside of cathode, kg/s
$P$	= discharge power, W
$R$	= representative interelectrode length, m
$R_a$	= anode inner radius, m
$R_c$	= keeper orifice radius, m
$r, \theta, z$	= cylindrical coordinates
$T_e$	= electron temperature, K
$\mathbf{u}$	= exhaust velocity vector, m/s
$u$	= exhaust velocity, m/s

$u_A$	= characteristic exhaust velocity due to applied magnetic field, m/s
$u_{\text{EXP}}$	= experimentally evaluated exhaust velocity, m/s
$u_s$	= characteristic exhaust velocity due to self-induced field, m/s
$V_d$	= discharge voltage, V
$V_k$	= keeper voltage, V
$V_{0,}$	= offset voltage, V
$V'_0$	= axial position of cathode tip, m
$z_c$	= axial position of cathode tip, m
$\alpha$	= characteristic parameter of applied-field thrust
$\eta$	= thrust efficiency, %
$\mu_0$	= permittivity in vacuum, A <sup>2</sup> · s <sup>4</sup> /kg · m <sup>3</sup>
$\sigma$	= electrical conductivity, 1/Ω · m

## Subscripts

–	= representative value
EXP	= experimentally fit value
RR	= rigid rotator model
TKV	= Tikhonov’s model

## I. Introduction

MAGNETOPLASMA DYNAMIC (MPD) thrusters generate thrust through propellant acceleration by the Lorentz force, which is generated by the interaction between a discharge current and a magnetic field. Similar to Hall thrusters, MPD thrusters accelerate quasi-neutral plasmas and are able to achieve a high thrust density. In a Hall thruster, the acceleration voltage and propellant flow rate primarily determine the thrust performance [1]. In practice, the propellant flow rate for efficient electrostatic acceleration, and hence the thrust density, are limited. In contrast, in an MPD thruster, the thrust is determined primarily by the discharge current and magnetic field strength, thereby having a potential of even higher thrust density [2]. The combination of a high-power supply with a compact thruster capable of high thrust-to-power ratio is an attractive option as a primary propulsion system for deep-space missions [3].

Two different types of MPD thrusters exist with respect to the magnetic field: the “self-field” type, in which the discharge current itself induces the magnetic field, and the “applied-field” type, in which a separate magnetic circuit applies the field. The self-field type does not require a separate magnetic circuit and allows a simple construction. However, obtaining sufficiently high electromagnetic thrust requires kiloampere-class discharge current [4]. This high-current operation leads to practical problems such as electrode erosion and requires discharge power in the range of 10<sup>0</sup>–10<sup>1</sup> MW [5], which is unfeasible in current state-of-the-art space-rated systems. Because of these issues, self-field MPD thrusters are not included in space propulsion development plans for the next 10 years

Received 7 January 2016; revision received 13 June 2016; accepted for publication 19 July 2016; published online XX epubMonth XXXX. Copyright © 2016 by the American Institute of Aeronautics and Astronautics, Inc. All rights reserved. Copies of this paper may be made for personal and internal use, on condition that the copier pay the per-copy fee to the Copyright Clearance Center (CCC). All requests for copying and permission to reprint should be submitted to CCC at www.copyright.com; employ the ISSN 0748-4658 (print) or 1533-3876 (online) to initiate your request.

\*Ph.D. Student, Department of Aerospace Engineering, Fro-cho, Chikusa-ku.  
†Graduate Student, Department of Aerospace Engineering, Fro-cho, Chikusa-ku.

‡Assistant Professor, Department of Aerospace Engineering, Fro-cho, Chikusa-ku. Member AIAA.

§Professor, Department of Aerospace Engineering, Fro-cho, Chikusa-ku. Associate Fellow AIAA.

[6]. In contrast, the applied-field type requires a lower discharge current than the self-field type, which negates the electrode erosion concern. Because of this advantage, applied-field type MPD thrusters are included in the near-future space development roadmap [7] and are considered to be suitable for high-power electric propulsion. This paper discusses applied-field magnetoplasmadynamic (AF-MPD) thrusters.

Several studies have been conducted to investigate the thruster performance and understand the acceleration mechanisms of axisymmetric-type AF-MPD thrusters. This type of thruster consists of a central, cylindrical cathode and a concentric, axisymmetric anode, and it undergoes steady-state or quasi-steady operation with a large pulsed-discharge current [8–15]. Myers et al. [8] examined steady-state operation characteristics at the 100 kW level for a wide range of geometries and various different operating conditions. They found that both thrust and thrust efficiency increased with increasing input power. Tikhonov et al. [9] used lithium as propellant. Owing to its low ionization energy, lithium reduces ionization losses; as a result, a thrust efficiency of 50% has been achieved. However, in conducting ground tests, lithium as a propellant requires an evaporator and poison-proof equipment such as protective clothing or respirators [10]. Besides these studies, several models have been proposed to make a scaling law of AF-MPD thruster operation characteristics. In addition, a semi-empirical thrust formula has been proposed, defining the thrust as the summation of three elements: applied-field thrust, self-field thrust, and gas-dynamic thrust. Fradkin et al. [13] proposed the “rigid rotor model”, which treats the generated plasma as a rigid rotating body with a constant angular velocity. According to this model, the electromagnetic thrust is proportional to the product of discharge current, magnetic field strength, and anode radius. Mikellides et al. [14] considered the effect of viscous friction force on the rigid rotor model. They found that the heavy particles are heated directly by viscous forces, and the main acceleration mechanism is the conversion of thermal energy to axially directed kinetic energy.

Iwakawa et al. [15] developed a two-dimensional AF-MPD thruster. A rectangular-shaped discharge channel generates a Lorentz force, in principle, parallel to the exhaust velocity and leads to high thrust efficiency. However, their thruster required at least 300 A of discharge current to maintain discharge under quasi-steady operating conditions. These operating conditions are not necessarily optimal for reducing electrode erosion.

A possible method of reducing ionization energy losses is increasing the discharge voltage and decreasing the relative ratio of ionization energy to discharge voltage. This is exactly the same concept as that used in Hall thrusters or ion engines. That is, an MPD thruster operating at a discharge voltage level of 100 V potentially has an increased thrust efficiency. An important difference between Hall thrusters and AF-MPD thrusters is that, in the case of Hall thrusters, the discharge voltage is preset, whereas in the case of AF-MPD thrusters, it is passively determined by other preset operation parameters such as discharge current, applied magnetic field, and propellant flow rate. The Lorentz force produced by the interaction between the discharge current and magnetic field is proportional to  $J_d^2$  in a self-field thruster [16] and to  $J_d \bar{B}$ , where  $\bar{B}$  is a representative value of the applied magnetic field, in an applied-field thruster [13]. Therefore, in principle, the ratio of the applied-field to self-field thrusts is proportional to  $\bar{B}/J_d$ ; this means that, if the contribution of an applied-field thrust dominates over a self-field thrust, low-current and high-voltage operation is possible. Increasing the ratio of the applied- to self-field thrusts is carried out by increasing  $\bar{B}$  while decreasing  $J_d$ . In arc discharge, the major charge carrier is thermionic electrons. Previous studies used a rod cathode made of thoriated tungsten. Using a conventional rod cathode, a discharge current of the order of  $10^2$  to  $10^4$  A was necessary to increase the cathode surface temperature forcibly to obtain thermionic electrons for maintaining arc discharge [17]. Myers et al. [18] measured the cathode surface temperature. With 12 mg/s of nitrogen as propellant and 875 A of discharge current, the surface temperature on the 2% thoriated tungsten rod cathode reached more than 3000 K. This high-temperature operation could cause severe cathode erosion and

shorten the thruster lifetime. In quasi-steady operation, the cathode surface temperature is typically low (with an average temperature less than 1000 K), and spotty arc attachment occurs [19]. This increases the local surface temperature of the cathode, resulting in a much higher erosion rate [20]. Such cold cathode conditions also occur during the startup phase of steady-state operation, until the surface temperature becomes sufficiently high for thermionic electron emission.

In this study, a thermionic electron emission-type hollow cathode was used in steady-state AF-MPD thrusters. Before starting the main discharge, the hollow cathode ran with a small propellant flow rate of about 0.2 mg/s and a keeper current of 2.0 A. Steady-state thruster operation was achieved at a discharge current level of up to 20 A, which is 10 to 1000 times lower than that of previous studies, while obtaining competitive thrust performance.

## II. Experimental Setup

In this study, both axisymmetric and rectangular-type AF-MPD thrusters were developed to evaluate their thrust performance. First, the experimental data obtained for each type of thruster will be presented, followed by an overall analysis of the thruster performances.

Figure 1 shows a diagram of the axisymmetric-type AF-MPD thruster. The thruster head comprises an axisymmetric anode, a hollow cathode on the central axis, insulators, and a solenoid coil. The anode is cylindrically shaped and made of copper, with the inner diameter varying from 52 to 80 mm in a conical transition. The hollow cathode (shown in Fig. 2) consists of a commercial emitter made of tantalum [21] (LHC-03AE1-01, Kaufman & Robinson Inc.), and its keeper electrode has a 2.0-mm-diam orifice. The solenoid coil applies the external magnetic field. Magnetic field strength distribution was measured using a Gauss meter (GM-4000, Denshijiki Industry Co. Ltd.). On the thruster axis, the maximum magnetic field strength was measured to be 265 mT at the center of the coil and 103 mT at the exit of the anode. One flow channel inside the emitter and two outside flow channels at 11 mm off-axis (Fig. 2 shows only one of the two outside flow channels) inject propellant into the discharge channel. The propellant mass flow rate through the hollow cathode is designated by  $\dot{m}_1$  and that through two off-axis supply channels by  $\dot{m}_2$ . In this paper,  $z$  designates the axial position originating at the anode exit. The position of the hollow cathode tip,

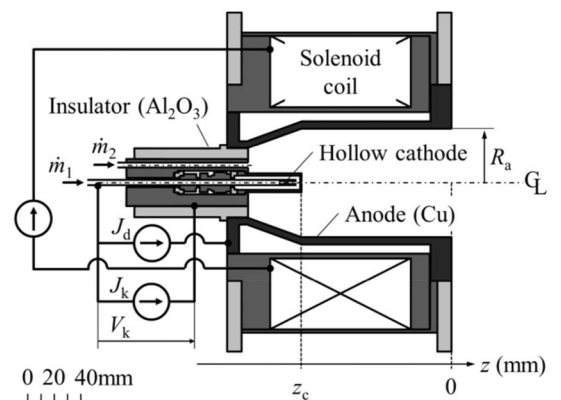


Fig. 1 Cross-sectional view and circuit diagram of axisymmetric thruster, type A.

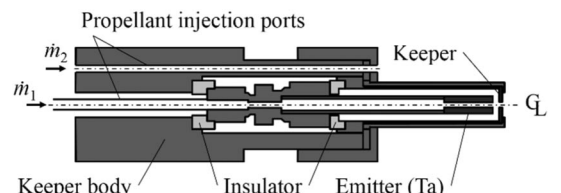


Fig. 2 Cross-sectional view of hollow cathode for type A thruster.

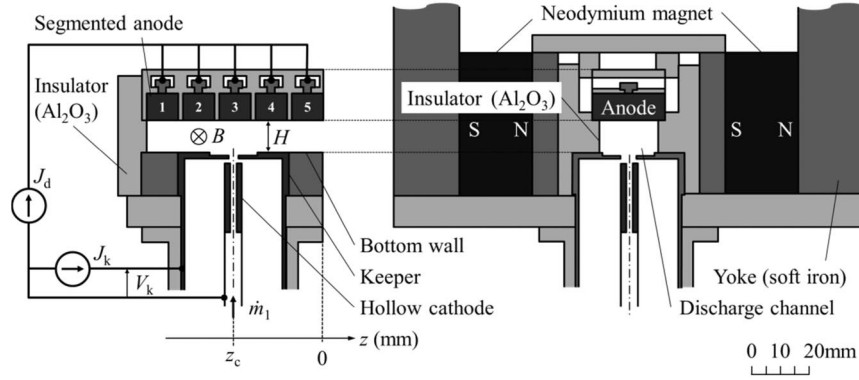


Fig. 3 Schematic of the rectangular thruster, type B1. Left: cross-sectional view and circuit diagram; right: frontal view.

$z_c$ , was set either at the anode exit ( $z_c = 0$  mm) or 105 mm upstream from the anode exit ( $z_c = -105$  mm). The center of the solenoid coil was set at  $z = -80$  mm. The anode and solenoid coil were water-cooled and could maintain steady operation at up to 6 kW.

Figure 3 shows a rectangular-type AF-MPD thruster (type B1). The discharge channel has a rectangular shape with a width of 20 mm and a length of 60 mm in the flow direction. The height of the discharge channel,  $H$ , was varied from 5 to 15 mm. The upper surface consists of an anode made of molybdenum, whereas the lower surface consists of a commercial hollow cathode (DLHC-1000, Kaufman & Robinson Inc.). Because the commercial hollow cathode has a keeper electrode with a large outer diameter (36 mm), the cathode center is set at  $z_c = -30$  mm. Two neodymium magnets (with a height of 50 mm, thickness of 25 mm, and length of 50 mm in the flow direction), which are connected by soft iron yokes, apply the magnetic field. The magnetic field strength was measured to be 240 mT at the center of the discharge channel,  $z = z_c = -30$  mm, gradually decreasing toward the exit of the discharge channel, and 160 mT at  $z = 0$  mm, the exit of the discharge channel. Although the anode is segmented into five pieces [22], the experimental data presented in this paper were obtained with them electrically connected together to form a single electrode.

Figure 4 shows a second rectangular-type AF-MPD thruster (type B2). For the cathode to be situated closer to the exit of the discharge channel, type B2 has a hollow cathode with a small outer size. The keeper electrode has a rectangular shape with a width of 25 mm and a length of 15 mm in the flow direction. This specially designed hollow cathode consists of the same emitter material as that used in the axisymmetric thruster shown in Figs. 1, 2 and a keeper electrode with a 3-mm-diam orifice. The rectangular-shaped discharge channel has 25 mm width, and the discharge channel height  $H$  was varied from 10 to 15 mm. Its upper surface consists of an anode with a width of 25 mm and a length of 15 mm in the flow direction. The same permanent magnets and yokes as in Fig. 3 apply the external magnetic field. The magnetic field strength was measured to be 200 mT at  $z = z_c = -9$  mm. In both type B1 and B2 thrusters, the flow channel

inside the hollow cathode emitter injects the entire quantity of propellant into the discharge channel.

Each thruster type (A, B1, and B2) was operated in a stainless-steel vacuum chamber with an inner diameter of 2 m and a length of 4 m [23]. During operation, a turbomolecular pump (3203LMC, Shimadzu Corporation) with a capacity of 3200 l/s and rotary pump (2100SD, Adixen Vacuum Products) with a capacity of 33 l/s evacuated the chamber. The ionization gauge (GI-TL3, ULVAC Technologies, Inc.) and Pirani gauge (GP-1S, ULVAC Technologies, Inc.) measured the pressure inside the chamber. The ultimate pressure was 1 mPa, whereas with propellant injection at a rate of 1.3 mg/s, the inside chamber pressure was maintained at approximately 55 mPa. A feedthrough, which was located at a chamber side flange, applied the discharge current, keeper current, and solenoid coil current.

A pendulum-type thrust stand of the same type as that described in [24], consisting of a stand arm, vacuum bellows, and two bearings, measured the thrust. The bellows and bearings were assembled on the vacuum chamber flange interfacing between the vacuum and the atmosphere. The radial load exerted onto the bearings was compensated by adjusting the vertical position of the bearings under operating conditions, so that the friction force exerted on the bearings, which degrades the thrust resolution, was effectively eliminated. The stand arm comprised copper tubes inside its body, through which cooling water and propellant were supplied. The pendulum displacement was amplified by a 1.1 m aluminum arm located outside the chamber and was sensed by a linear variable differential transformer (LVDT1301-2, Shinko Electric Co., Ltd.). The thrust stand was calibrated using an arrangement of weights, a pulley, and a dc motor under identical vacuum conditions to those during thruster operations [23]. The dc motor rotated the pulley to change the number of weights and vary the load applied to the thruster. The mass of weights was measured using an electric balance (AW320, Shimadzu Corporation). As the load was varied, the signal voltage of a differential transformer was measured three times. The average value for each load was fitted by a least-square method, and a regression line was estimated. From 0 to 49 mN of load, a linearity

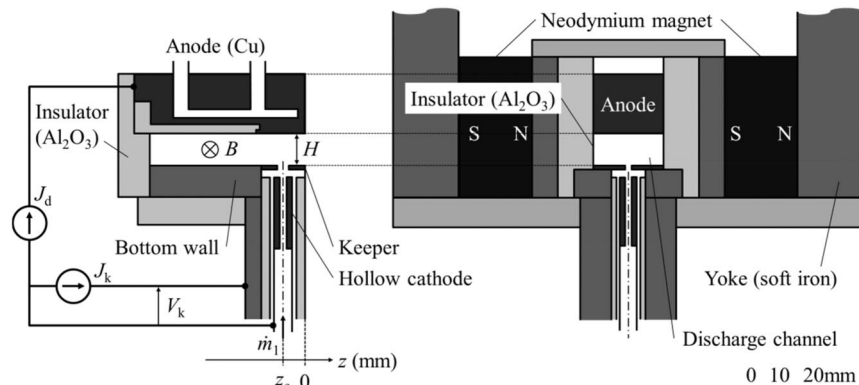


Fig. 4 Schematic of the rectangular thruster, type B2. Left: cross-sectional view and circuit diagram; right: frontal view.

was confirmed with the regression line having a correlation coefficient of 0.997. For this calibration, the effect of mass measurement error on calibration factor was  $\pm 0.02$  mN/V. This corresponds to  $\pm 2.0 \times 10^{-3}$  mN, which is 0.01% of the thrust range of 26 mN measured in this study. The thrust stand arm oscillated about the fulcrum with an oil dumper, yet without a feedback control system. Operating the vacuum pumps and supplying cooling water for the anode and solenoid coil, the gauge head of the a linear variable differential transformer oscillated with an amplitude of 0.8 mm. Owing to this oscillation, the thrust stand resolution was 0.2 mN, which was 0.8 and 5% of the measured maximum and minimum thrust value, respectively.

The electromagnetic interaction force, otherwise known as the ‘‘tare force’’  $F_{\text{tare}}$ , was produced among the lead wires supplying a discharge current  $J_d$  and a solenoid coil current  $J_c$ , which corresponded experimentally to the following equation:

$$F_{\text{tare}} = c_1 J_d + c_2 J_c + c_3 J_d^2 + c_4 J_d J_c + c_5 J_c^2 \quad (1)$$

To evaluate  $F_{\text{tare}}$ , the thrust was measured while shorting the anode and cathode, and the coefficients  $c_1$  to  $c_5$  were determined by the least-square method. A dc power supply (N8761A, Keysight Technologies) was used for supplying  $J_c$ . Based on the coefficient of determination of the tare force fitting curve, the accuracy of thrust measurement was  $\pm 0.01$  mN.

A data logger (cDAQ-9178, National Instruments) and oscilloscope (DL750, Yokogawa Meters & Instruments Corporation) recorded all experimental data.

### III. Results and Discussions

#### A. Experimental Method

Table 1 summarizes the operating conditions used in this experiment. In the table,  $\dot{m}$  represents the total propellant mass flow rate;  $\dot{m} \equiv \dot{m}_1 + \dot{m}_2$  in the type A thruster, whereas  $\dot{m} \equiv \dot{m}_1$  in the type B thrusters. The representative value of the applied magnetic field  $\bar{B}$  is equal to the value at the coil center. The values for thrust  $F$ , discharge voltage  $V_d$ , and keeper voltage  $V_k$  were measured, whereas  $\dot{m}_1$ ,  $\dot{m}_2$ ,  $J_d$ ,  $\bar{B}$ ,  $H$ , and  $z_c$  were variable control parameters. Because operating the thruster causes a nonnegligible thermal drift in the thrust stand, the displacement before and after steady-state arc discharge operation for each operating condition was measured, and the difference was converted to thrust. This was carried out using the correction method described in Sec. II, consisting of subtracting the tare force from the apparent thrust to obtain the net thrust. During the measurement,  $\dot{m}$  and  $\bar{B}$  were kept constant. The cold flow thrust, which was measured in advance, was added to obtain the total thrust. To obtain the thrust data, the thruster was operated at least for 4 s before turning off the discharge current. During this time, the ratio of the rms of discharge current to the time averaged value was also evaluated. In this study, when this ratio was less than 10%, the operation was categorized as ‘‘stable’’. The uncertainties obtained for  $\dot{m}$ ,  $J_d$ ,  $\bar{B}$ ,  $R_d$  or  $H$ , and measured  $V_d$  were  $\pm 6.2 \times 10^{-2}$  mg/s,  $\pm 51$  mA,  $\pm 10$  mT,  $\pm 0.1$  mm, and  $\pm 2.0$  V, respectively. In the following figures, in which experimental results are plotted, the symbol represents the time-averaged value, and the error bar represents the rms with a 68% confidence interval.

**Table 1** Operating conditions

Parameter	Type A	Type B1	Type B2
$\dot{m}_1$ , mg/s	0.83–2.10	0.83–2.10	0.83–2.10
$\dot{m}_2$ , mg/s	0–3.10	0	0
$\dot{m}$ , mg/s	0.83–3.90	0.83–2.10	0.83–2.10
$J_d$ , A	10–20	5–15	5–15
$\bar{B}$ , mT	133–265	240	200
$R_d$ , mm	40	—	—
$H$ , mm	—	10, 15	10, 15
$z_c$ , mm	0, –105	–300	–9

#### B. Operating Conditions

Zhurin et al. [25] presented the operating characteristics of an axisymmetric-type MPD thruster with applied magnetic field (they named it a ‘‘high-current end-Hall thruster’’) and with a discharge current of up to 8 kA, in which the self-field thrust was treated as the dominant thrust component. They used the flow Mach number, the ratio of the self-field thrust to the gas-dynamic thrust, and the ratio of flow velocity to  $E \times B$  drift velocity as dimensionless, characteristic quantities. Their formulas contain a term proportional to  $J_d^2$  for the self-field thrust and another term for the gas-dynamic thrust. However, as will be shown in the following discussions, their formulas do not apply to the present thruster performance because these terms are negligible in this study. In contrast, in an axisymmetric-type AF-MPD thruster, if the swirl acceleration is dominant, the thrust is proportional to the radius of the acceleration region [13]. In a rectangular-type AF-MPD thruster, in principle, the thrust is proportional to the height of the acceleration region [22]. In both types, the characteristic applied-field thrust  $F_A$  is expressed by the following equation:

$$F_A \equiv J_d \bar{B} R \quad (2)$$

where  $R$  is a representative interelectrode distance. On the other hand, the self-field thrust [16] is characterized by the following equation:

$$F_S \equiv \mu_0 J_d^2 \quad (3)$$

Based on Eqs. (2) and (3), the ratio  $\alpha$  of the applied-field to self-field thrust, which is a representative values of operating conditions in an acceleration region, is given by

$$\alpha \equiv \frac{J_d \bar{B} R}{\mu_0 J_d^2} = \frac{\bar{B} R}{\mu_0 J_d} \quad (4)$$

To obtain real thrust components,  $F_A$  and  $F_S$  should be multiplied by their respective, effective factors. However,  $\alpha$  still represents the relative contribution of an applied to self-magnetic thrust because its order of magnitude does not vary by this factorization. Table 2 provides a summary comparing the operating conditions of this study with those of previous studies with respect to the value of  $\alpha$ . In the table, A, B1, and B2 represent the type A and type B thrusters tested in this study. Meanwhile, C to G represent thrusters tested in previous studies, where C to F are axisymmetric types and G is a rectangular-type AF-MPD thruster. As can be seen from the table, in the previous studies,  $\alpha$  was in the approximate range of 0.1–50. However, in this study,  $\alpha$  even exceeded 800, which suggests that the applied-field thrust should be dominant in the experiments presented in this paper.

#### C. Operating Characteristics of Type A Thruster

In this section, the experimentally obtained exhaust velocity that was estimated based on the measured thrust as well as discharge voltage characteristics of the type A thruster will be shown and compared with several models and operating characteristics found in previous studies. From Eq. (2), the characteristic exhaust velocity  $u_A$  of the applied-field thrust, which is evaluated using only preset operating parameters, is defined as

$$u_A \equiv \frac{F_A}{\dot{m}} = \frac{J_d \bar{B} R}{\dot{m}} \quad (5)$$

The experimental exhaust velocity  $u_{\text{EXP}}$  is defined as the ratio of the experimentally measured thrust to the total mass flow rate:

$$u_{\text{EXP}} \equiv \frac{F_{\text{EXP}}}{\dot{m}} \quad (6)$$

The coefficient  $c_{\text{EXP}}$  is defined by

**8** Table 2 Operating ranges

Data set	A	B1	B2	C	D	E	F	G
Configuration Reference	Axisymmetric	Rectangular	Rectangular	Axisymmetric Myers et al. [7]	Axisymmetric Tikhonov et al. [8]	Axisymmetric Tahara et al. [11]	Axisymmetric Sasoh and Arakawa [12]	Rectangular Iwakawa et al. [15]
$J_d$ , kA	0.01–0.02	0.005–0.015	0.005–0.015	0.75–1	6.5–16.5	1.2–2.9	0.085–0.2	0.13–0.3
$\bar{B}$ , mT	133–265	243	200	30–165	38–190	45–90	25–250	211–1130
$\dot{m}$ , mg/s	0.83–3.9	0.83–2.1	0.83–2.1	25–100	400	45–126	0.9–9	200
$P$ , kW	0.76–3.26	0.59–3.34	0.46–3.0	23–96	53–186	—	3–9.8	49–173
$P/\dot{m}$ ( $\times 10^9$ ), $\text{m}^2/\text{s}^2$	0.23–3.91	0.31–15.6	0.22–3.06	0.2–2.5	0.9–1.7	—	0.3–11	0.24–0.87
$\alpha$	210–840	130–570	110–480	0.7–3.5	1–4.7	0.13–0.28	2.2–51	12–32

$$c_{\text{EXP}} \equiv \frac{F_{\text{EXP}}}{F_A} = \frac{u_{\text{EXP}}}{u_A} \quad (7)$$

Figures 5a, 5b show  $u_{\text{EXP}}$  vs  $u_A$ . In the type A thruster,  $R = R_a$ , and  $\bar{B}$  is substituted with the value at the coil center. As can be seen in the figure,  $u_{\text{EXP}}$  is almost proportional to  $u_A$  regardless of the cathode position  $z_c$ , although the values of  $c_{\text{EXP}}$  differ. Note here that  $\bar{B}$  is larger in the case of  $z_c = -105$  (Fig. 5a) than in the case of  $z_c = 0$  (Fig. 5b).

The interaction between the radial part of the discharge current and the axial part of the magnetic field gives rise to the Lorentz force in the azimuthal direction. This Lorentz force leads to a swirl motion. In Fradkin's rigid rotator (RR) model [13], plasma in the torque generation region is treated as a rigid rotator without a friction force. In downstream, increasing the rotator radius along the solid or magnetic nozzle, the rotational kinetic energy is transferred to axial

kinetic energy, while conserving the kinetic energy and angular momentum. This energy transfer leads to the thrust represented by

$$F_{\text{RR}} = c_{\text{RR}} J_d \bar{B} R_a \quad (8)$$

$$c_{\text{RR}} = \frac{1}{\sqrt{2}} \left[ 1 - \frac{3}{2} \left( \frac{R_c}{R_a} \right)^2 \right] \quad (9)$$

Here, in the ideal case, the proportionality coefficient  $c_{\text{RR}}$  is a function of the effective ratio of the cathode outer radius to the anode inner radius  $R_c/R_a$ . In the type A thruster, substituting  $R_a = 40$  mm and the keeper orifice radius  $R_c = 1$  mm,  $c_{\text{RR}} \approx 2^{-1/2}$ . From Eqs. (5) and (8), the exhaust velocity characteristics of the rigid rotator model are evaluated by

$$u_{\text{RR}} \equiv \frac{F_{\text{RR}}}{\dot{m}} = c_{\text{RR}} u_a \quad (10)$$

From Tikhonov et al.'s semi-empirical formula [26], the thrust, which is the sum of the applied-field thrust, gas-dynamic thrust with a solid nozzle, and self-field thrust, is given by

$$F_{\text{TKV}} \equiv c_{\text{TKV}} J_d \bar{B} R_a + c'_{\text{TKV}} a_0 \dot{m} + \frac{\mu_0 J_d^2}{4\pi} \left[ \frac{3}{4} + \ln \left( \frac{R_a}{R_c} \right) \right] \quad (11)$$

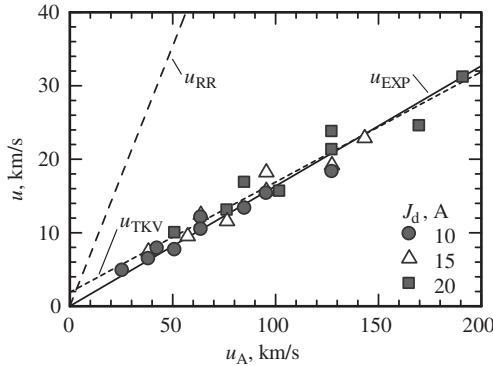
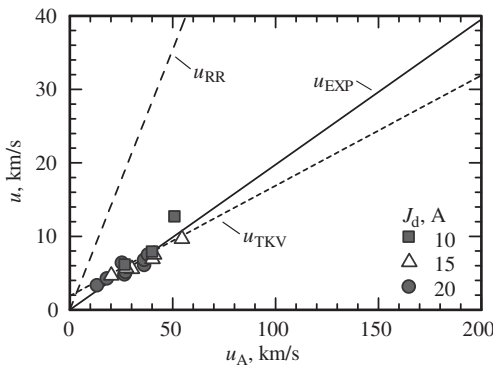
In this experiment, the maximum value of the discharge current was 20 A, and the self-field thrust was less than 0.17 mN, which is no more than 0.9% of the total thrust. Based on these results, the third term on the right-hand side of Eq. (11) is negligible. Therefore,

$$F_{\text{TKV}} \cong c_{\text{TKV}} J_d \bar{B} R_a + c'_{\text{TKV}} a_0 \dot{m} \quad (12)$$

Using the same assumptions as in [26] that the electron temperature  $T_e$  is 1.5 eV, and the ion temperature is much lower than  $T_e$ , the ion acoustic speed  $a_0 \approx (kT_e/M_i)^{1/2}$  is 1.9 km/s. Using this value, the coefficients of Eq. (12) are estimated as  $c_{\text{TKV}} \sim 0.15$ ,  $c'_{\text{TKV}} \sim 1$ . From Eq. (12), the exhaust velocity characteristics of Tikhonov's model  $u_{\text{TKV}}$  is represented by

$$u_{\text{TKV}} = \frac{F_{\text{TKV}}}{\dot{m}} \equiv c_{\text{TKV}} u_a + c'_{\text{TKV}} a_0 \quad (13)$$

Figures 5a, 5b also show the plots for  $u_{\text{RR}}$  and  $u_{\text{TKV}}$ . Based on Eq. (7), the experimental data are applicable to  $c_{\text{EXP}} = 0.16$  and 0.20 for  $z_c = -105$  mm and 0 mm, respectively. The experimental exhaust velocity  $u_{\text{EXP}}$  shows a similar tendency to that of  $u_{\text{RR}}$ , although the effective factor is no more than 22–29% of that of  $u_{\text{RR}}$ . In the rigid rotator model, a nonviscous, fully ionized plasma that moves along the magnetic field line is assumed, whereas momentum losses due to viscous shear and radial diffusion are not considered. Moreover, in practice, the effective rotation radius should be smaller than the anode inner radius. Therefore,  $u_{\text{EXP}}$  can become much lower than  $u_{\text{RR}}$ .


 a)  $z_c = -105$  mm,  $c_{\text{EXP}} = 0.16$ 

 b)  $z_c = 0$  mm,  $c_{\text{EXP}} = 0.20$ 

**9** Fig. 5 Exhaust velocity characteristics, type A ( $\dot{m}_1 = 0.83\text{--}2.1$  mg/s,  $\dot{m}_2 = 0\text{--}3.1$  mg/s,  $J_d = 10\text{--}20$  A,  $\bar{B} = 133\text{--}265$  mT,  $R_a = 40$  mm,  $R_c = 1$  mm), EXP: experimental value; RR: rigid rotator model [Eq. (10),  $c_{\text{RR}} = 2^{-1/2}$ ]; TKV: Tikhonov's semi-empirical formula [Eq. (13),  $c_{\text{TKV}} = 0.15$ ,  $c'_{\text{TKV}} = 1$ ,  $T_e = 1.5$  eV,  $a_0 = 1.9$  km/s]. The uncertainties of  $u_A$  and  $u_{\text{EXP}}$  were no more than  $\pm 3.0$  and  $\pm 10\%$  of the measured values, respectively.

Neglecting the Hall effect and ion slip, the generalized Ohm's law is given by

$$\mathbf{j} = \sigma(\mathbf{E} + \mathbf{u} \times \mathbf{B}) \quad (14)$$

In the rigid rotator model, each component in Eq. (14) can be expressed as  $\mathbf{j} = j_r$ ,  $\mathbf{E} = E_r$ ,  $\mathbf{B} = B_z$ , and  $\mathbf{u} = u_\theta$  using the cylindrical coordinate system. Using Eq. (14), the discharge voltage is expressed as

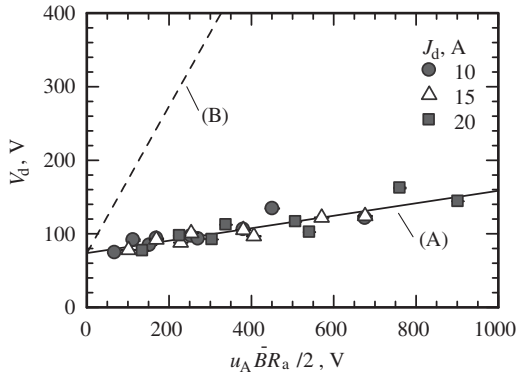
$$\begin{aligned} V_d &= V_0' - \int_{R_c}^{R_a} E_r dr \cong V_0' + \int_{R_c}^{R_a} \left( u_\theta B_z - \frac{j_r}{\sigma} \right) dr \\ &\equiv V_0 + c_v \frac{u_A \bar{B} R_a}{2} \end{aligned} \quad (15)$$

$V_0$  represents the sum of the plasma's electrical resistance and sheath potential drops.  $u_A \bar{B} R_a / 2$  is the representative value of the back electromotive force [27]. In the rigid rotator model,  $c_v$  is expressed as

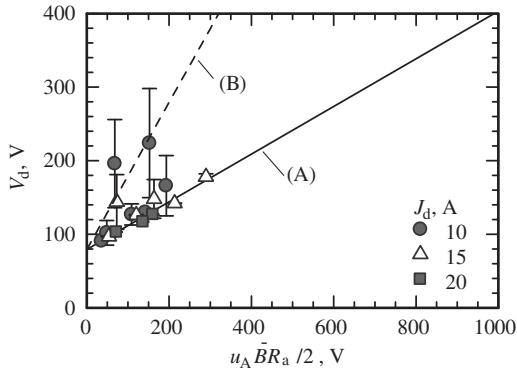
$$c_{v,RR} \equiv \left[ 1 - 3 \left( \frac{R_c}{R_a} \right)^2 \right] \quad (16)$$

Substituting the keeper orifice radius for  $R_c$  (equal to 1 mm),  $c_{v,RR} \approx 1.0$ .

Figures 6a, 6b show graphs of  $V_d$  vs  $u_A \bar{B} R_a / 2$ . As can be seen from the figure,  $V_d$  increases almost linearly with  $u_A \bar{B} R_a / 2$ . The rigid rotator model neglects the effect of viscosity; therefore, owing to viscosity, the effective value of  $c_v$  is smaller than that of  $c_{v,RR}$ . In this experiment, the effective value of  $c_v$  was estimated by curve fitting based on Eq. (15) and is represented as  $c_{v,EXP}$ . The fitted line is shown as the solid line (A), and the dashed line (B) shows the case for  $c_v = c_{v,RR}$ . Only stable operating conditions, with rms values



a)  $z_c = -105$  mm,  $c_{v,EXP} = 0.084$ ,  $V_0 = 74$  V



b)  $z_c = 0$  mm,  $c_{v,EXP} = 0.32$ ,  $V_0 = 79$  V

**Fig. 6 Voltage characteristics, type A** ( $\dot{m}_1 = 0.83\text{--}2.1$  mg/s,  $\dot{m}_2 = 0\text{--}3.1$  mg/s,  $J_d = 10\text{--}20$  A,  $\bar{B} = 133\text{--}265$  mT,  $R_a = 40$  mm): a) experimentally fit to Eq. (15), and b) rigid rotator model ( $c_{v,RR} \approx 1.0$ ) from Eqs. (15) and (16). The uncertainty of  $V_d$  was no more than  $\pm 2.7\%$  of the measured value.

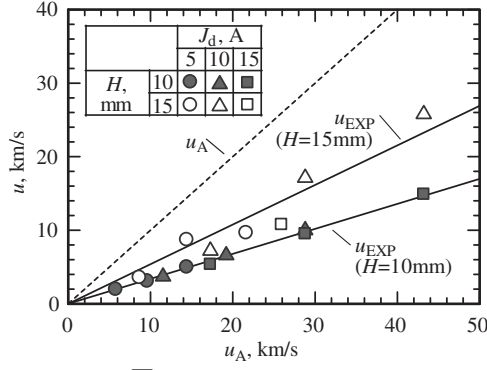
(shown by the magnitude of the error bar) lower than 10% of the time-averaged value during thruster operation (shown by the symbol), were employed to the fit, thereby yielding  $c_{v,EXP} = 0.084$ ,  $V_0 = 74$  V at  $z_c = -105$  mm; and  $c_{v,EXP} = 0.32$ ,  $V_0 = 79$  V at  $z_c = 0$  mm. For increasing  $u_A \bar{B} R_a / 2$ , the ratio of  $V_0$  to  $V_d$  decreases, becoming 45% for both  $z_c = -105$  mm and  $z_c = 0$  mm. Therefore, for increasing  $u_A \bar{B} R_a / 2$ , the contribution of the electromagnetic thrust generation in the power consumption increases.

In [14], with  $\dot{m} = 100$  mg/s (argon),  $\alpha \sim 1$  ( $J_d = 1$  kA,  $\bar{B} \sim 40$  mT,  $R_a = 51$  mm,  $z_c = 0$  mm), the azimuthal Lorentz force causes the plasma to rotate and induces a shear force. This shear force and Joule heating due to kiloampere-order discharge current causes the heavy particle temperature to increase by up to 5 eV and transfer the internal energy to kinetic energy through the expansion along the magnetic nozzle. In this case, the azimuthal torque increases as  $J_d \bar{B} R_a$  increases, but the shear force also increases. Therefore, the azimuthal velocity should saturate so that  $u_A \bar{B} R_a / 2$  and  $V_d$  are proportional to  $\bar{B}$ . On the other hand, under the conditions of this experiment, in which  $\dot{m} \sim 3.9$  mg/s and  $\alpha \sim 100$  ( $J_d \sim 20$  A,  $\bar{B} \sim 265$  mT,  $R_a = 40$  mm),  $V_d$  is proportional to both  $u_A / 2$  and  $\bar{B} R_a$ . As a result,  $V_d$  is a linearly increasing function of  $\bar{B}^2$ . Assuming that limiting the discharge current to 20 A suppresses heavy particle heating by decreasing the Joule heating,  $u_\theta$  and  $u_A \bar{B} R_a / 2$  increase as  $J_d \bar{B} R_a$  increases. In the rigid rotator model, the plasma is assumed to act as a rigid rotator by an azimuthal Lorentz force  $J_d B_z R_a$  and expand through a diverging magnetic field. Owing to this expansion, the rotational energy is converted to axial kinetic energy. In the case that the work done by the azimuthal Lorentz force is completely converted to rotational energy before the axial kinetic energy conversion, the ion's Larmor radius would become 37 mm with an ion rotational kinetic energy of 70 eV at  $\bar{B} = 200$  mT. In reality, the plasma rotates in the azimuthal direction and at the same time expands through the diverging magnetic field. Therefore, the energy conversion from rotational energy to axial kinetic energy must occur simultaneously. Moreover, the viscous friction force accompanying the rotation is affected by the ions, and some portion of the rotational energy is converted to thermal energy. Therefore, the estimated value of  $c_{v,EXP}$  is no more than 32% of  $c_{v,RR}$ . As with the rotational-kinetic energy conversion, the energy conversion from thermal energy to axial kinetic energy must occur simultaneously. As a result, the "effective" Larmor radius should be much smaller than the preceding overestimation. In the same manner,  $V_d$  is expressed in terms of the quantity  $u_A \bar{B} R_a / 2$ , and this results in the characteristic current-voltage behavior observed in  $F_A$ -dominant, high- $\alpha$  operation. Verifying the preceding assumptions requires measurement of the azimuthal plasma velocity, the heavy particle temperature, and the discharge voltage, which is beyond the scope of this paper.

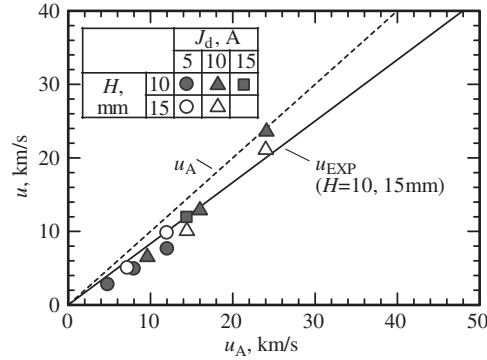
#### D. Operating Characteristics of Type B Thrusters

In the rectangular-type AF-MPD thrusters (type B), if the discharge current has a component only normal to the electrode and the plasma flow does not collide against the discharge channel wall, the Lorentz force (i.e., the thrust) and the exhaust velocity are given by Eqs. (2) and (5), respectively. In this case,  $R = H$ , and if  $u_{EXP} = u_A$ ,  $c_{EXP}$  should be unity.

Figures 7a, 7b shows  $u_{EXP}$  vs  $u_A$ . As with the type A thruster,  $u_{EXP}$  is a linear increasing function of  $u_A$  regardless of  $z_c$ . The figure also shows the linear fit of  $u_{EXP}$  based on Eq. (7). For the type B1 thruster, as shown in Fig. 7a,  $c_{EXP}$  varies with  $H$  such that  $c_{EXP} = 0.34$  and 0.54 for  $H = 10$  and 15 mm, respectively. The momentum loss in the type B thruster is mainly affected by the geometrical relationship between the Lorentz force vector and the discharge channel wall [22]. In the type B thruster, the volume integrated value of the  $z$  component of the Lorentz force does not depend on the discharge current path. However, if collisions of the propellant against the discharge channel wall occur, the thrust could become smaller due to momentum exchange. The Hall effect causes the generation of a discharge current component in the  $z$  direction, which interacts with the applied magnetic field to yield a Lorentz force component perpendicular to



a) Type B1,  $\bar{B} = 240$  mT,  $c_{\text{EXP}} = 0.34, 0.54$  for  $H = 10, 15$  mm, respectively

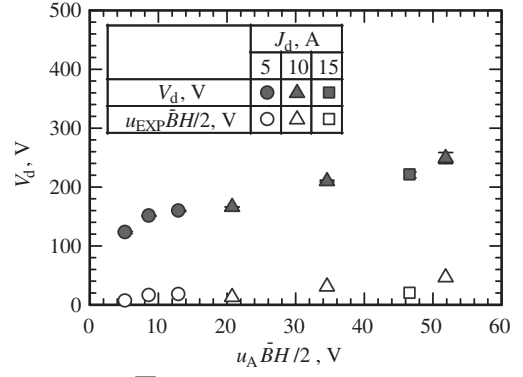


b) Type B2,  $\bar{B} = 200$  mT,  $c_{\text{EXP}} = 0.83$  for  $H = 10, 15$  mm

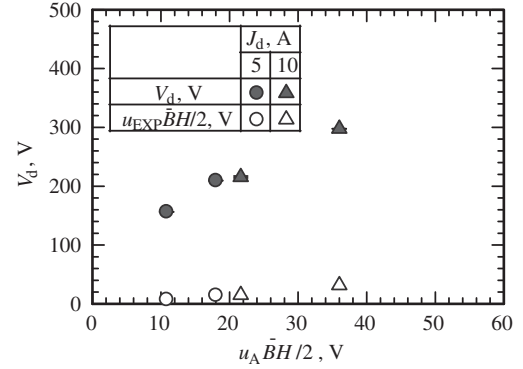
Fig. 7 Exhaust velocity characteristics of type B thruster ( $\dot{m}_1 = 0.83\text{--}2.1$  mg/s,  $J_d = 5\text{--}15$  A,  $\bar{B} = 200, 240$  mT,  $H = 10, 15$  mm). EXP: experimentally fit to Eq. (7). The uncertainties of  $u_A$  and  $u_{\text{EXP}}$  were no more than  $\pm 3.0$  and  $\pm 12\%$  of the measured value, respectively.

the wall. Therefore, part of the propellant collides against the discharge channel wall, producing a momentum loss. On the other hand, in the type B2 thruster, the discharge current distribution should shift downstream near the exit. The rate of collisions should therefore decrease. As a result,  $c_{\text{EXP}}$  became much higher, with a value of 0.83 regardless of  $H$ . In particular, at  $u_A = 24$  km/s,  $u_{\text{EXP}}$  reached as high as 98% of  $u_A$ .

Figure 8a, 8b shows  $V_d$  vs  $u_A \bar{B} R_a / 2$ . As can be seen in the figure,  $V_d$  increases linearly with  $u_A \bar{B} R_a / 2$  and reached values of 249 and 297 V for the type B1 and B2 thrusters, respectively. As mentioned previously, high-voltage operation decreases the relative ratio of ionization energy (15.8 eV for argon) to discharge voltage, giving values of 6.3 and 5.3% in the type B1 and B2 thrusters, respectively. Zuin et al. [28] reported that, at a given value of  $\bar{B}$ , a significant fluctuation level is observed only when  $J_d$  is larger than a threshold value (onset mode). This operating mode transition is reflected in the  $J_d$ - $V_d$  characteristic. When the onset mode occurs, the rate of discharge voltage increment with respect to discharge current,  $dJ_d/dV_d$ , rapidly increases, thereby forming a “kink.” Uribarri et al. [29] measured the onset voltage hash in a self-field MPD thruster. As  $J_d$  increases,  $V_d$  increases, and above the critical discharge current,  $V_d$  oscillates intensely in the range of 400–600 V with spike amplitudes nearly 100% of the baseline from which they rise, largely due to double charge ionization. In this experiment, as shown in Fig. 8,  $V_d$  increased linearly with  $J_d$  ( $V_d$  increased with  $u_A \bar{B} R_a / 2$ , and  $u_A$  was proportional to  $J_d$ ). The maximum value obtained for  $V_d$  was  $297 \pm 10$  V (type B2 thruster,  $\dot{m}_1 = 0.83$  mg/s,  $J_d = 10$  A,  $\bar{B} = 200$  mT,  $H = 15$  mm). Because  $V_d$  was below the aforementioned range (400–600 V), the onset phenomenon was not observed. The figure also shows effective back electromotive force  $u_{\text{EXP}} \bar{B} H / 2$ . For the operating conditions of the type B thrusters,  $u_{\text{EXP}} \bar{B} H / 2$  achieved a maximum of 46 V, which is 18% of  $V_d$



a) Type B1,  $\bar{B} = 240$  mT



b) Type B2,  $\bar{B} = 200$  mT

Fig. 8 Discharge voltage characteristics of type B thrusters ( $\dot{m}_1 = 0.83\text{--}2.1$  mg/s,  $J_d = 5\text{--}15$  A,  $\bar{B} = 200, 240$  mT,  $H = 10, 15$  mm). EXP: experimentally fit to Eq. (7). The uncertainties of  $u_A$  and  $u_{\text{EXP}}$  were no more than  $\pm 3.0$  and  $\pm 12\%$  of the measured value, respectively.

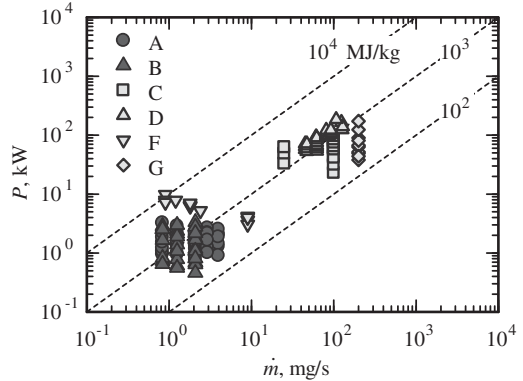
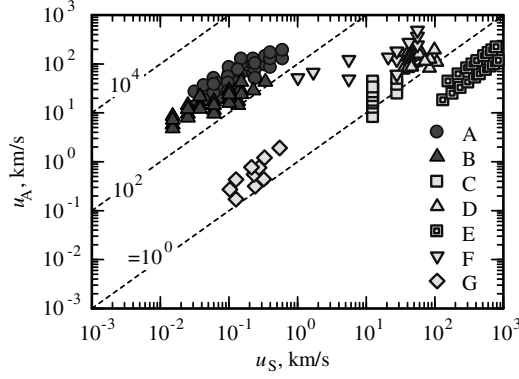


Fig. 9 Input power and propellant flow rate range. A to G correspond to the same symbols as those used in Table 2; B refers to B1 and B2. The uncertainties of  $\dot{m}$  and  $P$  were no more than  $\pm 7.4$  and  $\pm 0.2\%$  of the measured value, respectively, for the type A and B thrusters.

(type B1 thruster,  $\dot{m} = 0.83$  mg/s,  $J_d = 10$  A,  $\bar{B} = 240$  mT,  $H = 15$  mm,  $V_d = 249$  V). This suggests that the Joule heating and sheath potential drops strongly affect  $V_d$ . Further investigations including plasma diagnostics are necessary to understand the plasma acceleration mechanisms more clearly.

### E. Operating Range Identification

The purpose of this section is to make comparisons between this work and previous studies with respect to operating conditions and thrust performance. Figure 9 shows a plot of  $P$  vs  $\dot{m}$ . In the figure, the letters A to G represent results from this study and previous studies, as indicated in Table 2. The figure does not include the data set of study



**Fig. 10** Characteristic exhaust velocity ranges. A to G corresponds to the same symbols as those used in Table 2; B refers to B1 and B2.

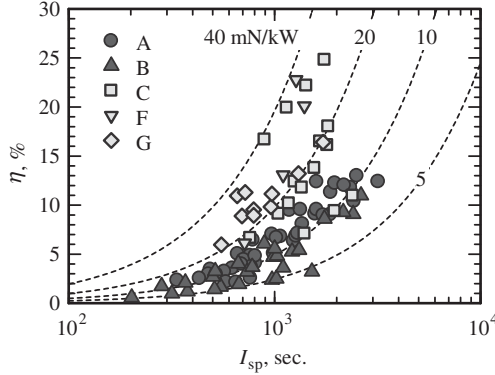


**Fig. 11** Thruster performances, propellant species Ar. A to G correspond to the same symbols as those used in Table 2; B refers to B1 and B2. The uncertainties of  $I_{sp}$  and  $\eta$  were no more than  $\pm 10$  and  $\pm 29\%$  of the measured value, respectively, for the type A thruster, and  $\pm 12$  and  $\pm 34\%$  of the measured value, respectively, for the type B thrusters.

E (Table 2) because the value of  $V_d$  is not indicated in the article. In this study (A, B1, and B2), the values of both  $\dot{m}$  and  $P$  were one to two orders of magnitude lower than those in the previous studies (C, D, G), but the specific power  $P/\dot{m}$ , in the range  $10^2$ – $10^4$  MJ/kg, is at almost the same level. As mentioned previously,  $10^2$ – $10^4$  A of  $J_d$  was necessary to obtain the thermionic electrons for keeping arc discharge using a conventional rod cathode. On this other hand, in this experiment, a thermionic-emission-type hollow cathode was used. Therefore, stable operation even with a small propellant flow rate (approximately 0.2 mg/s) and a small current ( $\sim 2$  A) was achieved. As a result, operating with a small propellant flow rate and small input power can yield the same specific power level as in the previous studies.

Figure 10 shows the characteristic velocity based on the applied-field thrust  $u_A$  [Eq. (5)] vs that of the self-field thrust  $u_s$ , given by

$$u_s \equiv \frac{F_s}{\dot{m}} \quad (17)$$

The dashed lines correspond to constant values of  $\alpha$ . As summarized in Table 2,  $\alpha$  obtained in this study (A, B1, and B2) was in the order of  $10^2$ , whereas that of previous studies (C–G) was in the order of  $10^{-1}$  to  $10^1$ . As can be seen from Eq. (2), applying a strong magnetic field ( $\sim 265$  mT) increases the applied-field thrust even when a hollow cathode supplies a small discharge current ( $\sim 20$  A). In this way, AF-MPD thruster operation was achieved at very high values of  $\alpha$ , which were higher than those reported in any previous study. In other words, operation was achieved in an applied-field-dominant condition.

The specific impulse  $I_{sp}$  and the thrust efficiency  $\eta$  are defined as

$$I_{sp} = \frac{u_{EXP}}{g} = \frac{F_{EXP}}{\dot{m}g} \quad (18)$$

$$\eta = \frac{F_{EXP}^2}{2\dot{m}P} = \frac{F_{EXP}^2}{2\dot{m}(J_d V_d + J_k V_k)} \quad (19)$$

These parameters are estimated based on the measured parameters  $F_{EXP}$ ,  $V_d$ , and  $V_k$ . Figure 11 shows the estimated values of  $I_{sp}$  and  $\eta$  of this study compared with those of previous studies, using argon as the propellant. Here, the effective propellant flow rate due to electrode erosion was not taken into account. For the type A and type B thrusters,  $I_{sp}$  was 330–3200 and 200–2600 s, respectively. In the data sets C, F, and G,  $I_{sp}$  was 460–2400 s. From Eqs. (18) and (19), it can be seen that the exhaust velocity is proportional to the square root of the specific power. Therefore, as shown in Fig. 11,  $I_{sp}$  and  $u_{EXP}$  are at the same level as in previous studies because  $P/\dot{m}$  is at the same level. However, the thrust-to-power ratio is lower by a factor of 2.

In this experiment, the thrust efficiency  $\eta$  of the type A and type B thrusters was at most 13 and 11%, respectively. These values are about half of those obtained in previous studies. To improve thrust efficiency, the impacts of  $J_d$  and  $\bar{B}$  on  $\eta$  were investigated by the analysis of variance (ANOVA) method [30]. In the ANOVA method, the observed variance in a particular variable is partitioned into components attributable to different sources of variation. Table 3 summarizes the ANOVA results for thrust and thrust efficiency based on typical operating conditions for the type A thruster. As can be seen from the table, both  $J_d$  and  $\bar{B}$  have a large variance ratio and exceed a 5% significance level of the Fisher–Snedecor distribution [31]. From Table 3a, it can be seen that  $J_d$  strongly correlates with  $F_{EXP}$  and has almost 70% contribution. On the other hand,  $\bar{B}$  has a lower percentage contribution than  $J_d$  to  $F_{EXP}$ . From the ANOVA results, it can be concluded that increasing  $J_d$  could be the most effective method of improving the thrust efficiency. As mentioned in Sec. II, a commercial-type thermionic electron emitter (LHC-03AE1-01, Kaufman & Robinson Inc.) was used. The current capability of the emitter was up to 20 A. Therefore, thruster operation and performance evaluation with currents of above 20 A (in other words, currents in the range of  $10^1$ – $10^2$  A) were not conducted. This could

**13** **Table 3** Analysis of variance results (type A thruster,  $\dot{m}_1 = 1.25$  mg/s,  $\dot{m}_2 = 0$  mg/s,  $J_d = 10$ –20 A,  $\bar{B} = 133$ –265 mT,  $R_a = 40$  mm,  $z_c = -105$  mm)

Source	Degree of freedom	Variation	Dispersion	Variance ratio	Net variation	Percent contribution, %
<i>Thrust</i>						
$J_d$	3	250	83.3	70.3	246	69.2
$\bar{B}$	3	103	34.4	29	100	28.1
Error	2	2.4	1.2	—	9.5	2.7
Total	8	355.4	—	—	355.4	100
<i>Thrust efficiency</i>						
$J_d$	3	38.5	12.8	24.8	37.0	52.9
$\bar{B}$	3	30.5	10.2	19.7	29.0	41.4
Error	2	1.0	0.5	—	4.0	5.7
Total	8	70.0	—	—	70.0	100

be realized through the development of a hollow cathode with a larger current capability.

The lifetime of a hollow cathode is limited by high-energy ion production in the so-called “plume mode” operation. Goebel et al. [32] concluded that the energetic ions were related to the plasma instabilities in the cathode plume and that proper selection of confining magnetic field strength tended to reduce the oscillations and energetic ion production. In the type A thruster, the electric field is parallel to the magnetic field at the hollow cathode position. Because the hollow cathode and solenoid coil are set coaxially, energetic ions should diffuse downstream through the diverging magnetic field. Therefore, the energetic ions are exhausted without wall surface impacts. Neither serious surface sputter nor erosion was observed after thruster operation. In the type B thruster, the anode and the hollow cathode are set face-to-face, and the magnetic field is perpendicular to the electric field. Although the operating characteristics of a hollow cathode and the operating mode transfer under this kind of electromagnet configuration have not been reported, there was no serious erosion detected on either the anode or the keeper surface after thruster operation. For developing a hollow cathode with larger current capability, the effect of the magnetic field in high-energy ion production should be considered, which is beyond the scope of this study and warrants further investigations.

#### IV. Conclusions

In this study, the operating characteristics of applied-field MPD thrusters, with a ratio of applied- to self-field thrusts  $\alpha$  in the range of  $10^2$ – $10^3$ , were investigated. Thrust and discharge voltage were expressed using the characteristic values of Lorentz force  $J_a \bar{B} R$  and back electromotive force  $u_a \bar{B} R_a / 2$ , respectively. Using a hollow cathode, applied-field thrust-dominant operation was achieved under the same specific power level ( $10^2$  –  $10^4$  MJ/kg) but with 10 to 100 times smaller mass flow rates than reported in previous studies. This was mainly achieved by the employment of a hollow cathode to maintain stable arc discharge at discharge current levels of up to 20 A. Even with a 10 A level of discharge current, a thrust efficiency of higher than 10% was obtained. Although thruster performance with a discharge current larger than 20 A could not be investigated, the present experimental results suggest that improved performance can be expected at discharge currents above this level, thereby warranting further investigations for validation.

#### References

- [1] Dannenmayer, K., and Mazouffre, S., “Elementary Scaling Relations for Hall Effect Thrusters,” *Journal of Propulsion and Power*, Vol. 27, No. 1, 2011, pp. 236–245.  
doi:10.2514/1.48382
- [2] Krulle, G., Auweter-Kurtz, M., and Sasoh, A., “Technology and Application Aspects of Applied Field Magnetoplasmadynamic Propulsion,” *Journal of Propulsion and Power*, Vol. 14, No. 5, 1998, pp. 754–763.  
doi:10.2514/2.5338
- [3] Sankaran, K., Cassady, L., Kodys, A. D., and Choueiri, E. Y., “A Survey of Propulsion Options for Cargo and Piloted Missions to Mars,” *Annals of the New York Academy of Sciences*, Vol. 1017, 2004, pp. 450–467.  
doi:10.1196/annals.1311.027
- [4] Choueiri, E. Y., “Scaling of Thrust in Self-Field Magnetoplasmadynamic Thrusters,” *Journal of Propulsion and Power*, Vol. 14, No. 5, 1998, pp. 744–753.  
doi:10.2514/2.5337
- [5] Choueiri, E. Y., and Ziemer, J. K., “Quasi-Steady Magnetoplasmadynamic Thruster Performance Database,” *Journal of Propulsion and Power*, Vol. 17, No. 4, 2001, pp. 967–976.  
doi:10.2514/2.5857
- [6] Saito, Y., Kinefuchi, K., Nagao, N., and Okita, K., “R&D Activities of Electric Propulsion in Japan,” *Proceedings of the 34th International Electric Propulsion Conf.*, IEPC Paper 2015-28, 2015.
- [7] Kinefuchi, K., Saito, Y., Nagano, N., Okita, K., Funaki, I., and Kuninaka, H., “Space Exploration Strategy with High Power Plasma Propulsions,” *Proceedings of the Plasma Conf. 2014*, 2014.
- [8] Myers, R. M., “Geometric Scaling of Applied-Field Magnetoplasmadynamic Thrusters,” *Journal of Propulsion and Power*, Vol. 11, No. 2, 1995, pp. 343–350.  
doi:10.2514/3.51431
- [9] Tikhonov, V. B., Semenikhin, S. A., and Polk, J. E., “Own Magnetic Field Impact on MPD Thrusters Performance with External Magnetic Field,” *Proceedings of the 26th International Electric Propulsion Conf.*, IEPC Paper 1999-176, 1999.
- [10] Lev, D. R., “Investigation of Efficiency in Applied Field Magnetoplasmadynamic Thrusters,” Ph. Dissertation, Dept. of Mechanical and Aerospace Engineering, Princeton Univ., Princeton, NJ, 2012.
- [11] Tahara, H., Kagaya, Y., and Yoshikawa, T., “Performance and Acceleration Process of Quasisteady Magnetoplasmadynamic Arcjets with Applied Magnetic Fields,” *Journal of Propulsion and Power*, Vol. 13, No. 5, 1997, pp. 651–658.  
doi:10.2514/2.5216
- [12] Sasoh, A., and Arakawa, Y., “Electromagnetic Effects in an Applied-Field Magnetoplasmadynamic Thruster,” *Journal of Propulsion and Power*, Vol. 8, No. 1, 1992, pp. 98–102.  
doi:10.2514/3.23448
- [13] Fradkin, D. B., Blackstock, A. W., Roehling, D. J., Stratton, T. F., Williams, M., and Liewer, K. W., “Experiments Using a 25-kW Hollow Cathode Lithium Vapor MPD Arcjet,” *AIAA Journal*, Vol. 8, No. 5, 1970, pp. 886–894.  
doi:10.2514/3.5783
- [14] Mikellides, P. G., Turchi, P. J., and Roderick, N. F., “Applied-Field Magnetoplasmadynamic Thrusters, Part 1: Numerical Simulations Using the MACH2 Code,” *Journal of Propulsion and Power*, Vol. 16, No. 5, 2000, pp. 887–893.  
doi:10.2514/2.5656
- [15] Iwakawa, A., Nakata, D., and Kuninaka, H., “Experimental Study of a Two-Dimensional Applied-Field Magnetoplasmadynamic Thruster,” *Transactions of the Japan Society for Aeronautical and Space Sciences, Aerospace Technology Japan*, Vol. 8, No. 27, 2010, pp. Pb\_13–Pb\_17.  
doi:10.2322/tastj.8.Pb\_13
- [16] Jahn, R. G., *Physics of Electric Propulsion*, McGraw-Hill, New York, 1968, Chap. 8.
- [17] Myers, R. M., and Soulas, G. C., “Anode Power Deposition in Applied-Field MPD Thrusters,” *28th AIAA/ASME/SAE/ASEE Joint Propulsion Conf. and Exhibit*, AIAA Paper 1992-3463, July 1992.
- [18] Myers, R. M., Suzuki, N., Kelly, A. J., and Jahn, R. G., “Cathode Phenomena in a Low-Power Magnetoplasmadynamic Thruster,” *Journal of Propulsion and Power*, Vol. 7, No. 5, 1991, pp. 760–766.  
doi:10.2514/3.23389
- [19] Nakata, D., Toki, K., Funaki, I., and Kuninaka, H., “Performance of ThO<sub>2</sub>-W, Y<sub>2</sub>O<sub>3</sub>-W and La<sub>2</sub>O<sub>3</sub>-W Cathodes in Quasi-Steady Magnetoplasmadynamic Thrusters,” *Journal of Propulsion and Power*, Vol. 27, No. 4, 2011, pp. 912–915.  
doi:10.2514/1.50412
- [20] Auweter-Kurtz, M., Glocker, B., Kurtz, H., Loesener, O., Schrade, H., Tubanos, N., Wegmann, T., Willer, D., and Polk, J., “Cathode Phenomena in Plasma Thrusters,” *Journal of Propulsion and Power*, Vol. 9, No. 6, 1993, pp. 882–888.  
doi:10.2514/3.23703
- [21] Kaufman, H. R., and Kahn, J. R., “Hollow Cathode Without Low-Work-Function Insert,” *Proceedings of the 29th International Electric Propulsion Conf.*, IEPC Paper 2005-47, 2005.
- [22] Ichihara, D., Harada, S., Kataoka, H., Yokota, S., and Sasoh, A., “Operation Characteristics of Steady-State, Applied Field, Rectangular Magnetoplasmadynamic (MPD) Thruster,” *Journal of the Japan Society for Aeronautical and Space Sciences*, Vol. 63, No. 2, 2015, pp. 37–44.  
doi:10.2322/jjsass.63.37 (in Japanese).
- [23] Yonemoto, M., and Sasoh, A., “Operation Characteristics of a Steady-State, Two-Dimensional MPD Thruster Using a Hollow Cathode,” *Transactions of the Japan Society for Aeronautical and Space Sciences, Aerospace Technology Japan*, Vol. 10, No. 28, 2012, pp. 7–12.  
doi:10.2322/tastj.10.Pb\_7
- [24] Sasoh, A., and Arakawa, Y., “A High-Resolution Thrust Stand for Ground Tests of Low-Thrust Space Propulsion Devices,” *Review of Scientific Instruments*, Vol. 64, No. 3, 1993, pp. 719–723.  
doi:10.1063/1.1144204
- [25] Zhurin, V. V., Popov, A. G., Porotnikov, A. A., Tikhonov, V. B., and Utkin, I. A., “The State of Research and Development of End-Hall Plasma Thrusters in the USSR,” *Proceedings of the 22nd International Electric Propulsion Conf.*, IEPC Paper 1991-080, 1991.
- [26] Tikhonov, V. B., Semenikhin, S., Brophy, J. R., and Polk, J. E., “The Experimental Performance of the 100 kW Li MPD Thruster with External Magnetic Field,” *Proceedings of the 24th International Electric Propulsion Conf.*, IEPC Paper 1995-105, 1995.

- [27] Sasoh, A., and Arakawa, Y., "Thrust Formula for Applied-Field Magnetoplasmadynamic Thrusters Derived from Energy Conservation Equation," *Journal of Propulsion and Power*, Vol. 11, No. 2, 1995, pp. 351–356.  
doi:10.2514/3.51432
- [28] Fisher, R. A., "The Logic of Inductive Inference," *Journal of the Royal Statistical Society*, Vol. 98, No. 1, 1935, pp. 39–82.  
doi:10.2307/2342435
- [29] Fisher, R. A., "On a Distribution Yielding the Error Functions of Several Well Known Statistics," *Proceedings of the International Congress of Mathematics*, Toronto, 1924, pp. 805–813.
- [30] Zuin, M., Cavazzana, R., Martines, E., Serianni, G., Antoni, V., Bagation, M., Andrenucci, M., Paganucci, F., and Rossetti, P., "Kink Instability in Applied-Field Magneto-Plasma-Dynamic Thrusters," *Physical Review Letters*, Vol. 22, 2004, Paper 225003.
- [31] Uribarri, L., and Choueiri, E. Y., "Relationship Between Anode Spots and Onset Voltage Hash in Magnetoplasmadynamic Thrusters," *Journal of Propulsion and Power*, Vol. 24, No. 3, 2008, pp. 571–577.  
doi:10.2514/1.34525
- [32] Goebel, D. M., Jameson, K. K., Katz, I., and Mikellides, I. G., "Potential Fluctuations and Energetic Ion Production in Hollow Cathode Discharges," *Physics of Plasmas*, Vol. 14, No. 10, 2007, Paper 103508.  
doi:10.1063/1.2784460

J. Blandino  
Associate Editor